

Characterization of carbon felt electrodes for vanadium redox flow batteries – A pore network modeling approach

R. Banerjee^{a,*}, N. Bevilacqua^a, L. Eifert^a, R. Zeis^{a,b}

^a Karlsruhe Institute of Technology, Helmholtz Institute Ulm, Helmholtzstraße 11, 89081, Ulm, Germany

^b Karlsruhe Institute of Technology, Institute of Physical Chemistry, Fritz-Haber-Weg 2, 76131, Karlsruhe, Germany

ARTICLE INFO

Keywords:

Pore network modeling
Vanadium redox flow battery
Carbon felt electrodes
Invasion percolation
Electrolyte saturation
Transport properties

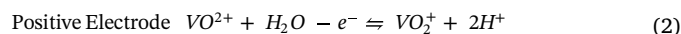
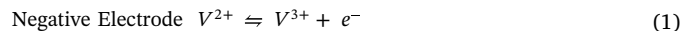
ABSTRACT

Carbon felt electrodes are commonly used as porous electrodes in Vanadium redox flow batteries for large-scale energy storage. The transport properties of these electrodes are an important parameter as the transport resistance can form a significant parasitic power loss depending on the configuration of the flow battery. Therefore, to better predict the overall parasitic power losses and devise strategies for the improvement of overall battery efficiency, the transport properties need to be properly understood. In this work, four commercially available carbon felt electrodes have been investigated for their transport properties. It has been shown that the non-activated electrode is hydrophobic in nature, while after activation, the electrodes become hydrophilic. The single-phase diffusion and permeability were found to decrease linearly with an increase in electrode thickness. The imbibition characteristics were similar for the four electrodes, although the change in wettability had a strong impact on the pressure required for the electrolyte to invade into the electrode.

1. Introduction

With the increased deployment of renewable sources of power generation, such as from wind and solar, there has been an increasing interest in large-scale energy storage solutions. It has been suggested that the electric grid would become unstable if the non-dispatchable contribution from renewable energy to the grid exceeded 20% of the overall capacity [1]. Among the different large-scale energy storage solutions available, redox flow batteries have gained popularity due to the deconvolution of the energy capacity and the power density available, and their ease of scalability [2,3]. A comparison of different grid-scale energy storage solutions is provided by Skyllas – Kazacos et al. [4] and Darling et al. [5]. The current status of development of redox flow batteries has been reviewed by several authors [2–7].

One of the chief concerns of redox battery chemistries is the cross-contamination of the electrolytes through the membrane, which could lead to irreversible reactions and thus lead to a reduction in energy capacity over time. This concern is alleviated in the all Vanadium redox flow (VRFB) coupling where both electrolytes are Vanadium based electrolytes [2]. Therefore, any cross contamination or crossover of ions through the membrane only results in power loss without any longer-term detrimental effects on the energy storage capacity. The half-cell reactions at the electrodes of the VRFBs are as shown below:



Zhou et al. [3] outlined the major types of resistances to transport involved in vanadium redox flow batteries (VRFBs), highlighting the charge transport overpotential and the mass transport overpotential as the two major sources of loss in performance, which need to be improved. In this work, the focus has been kept on the mass transport losses incurred in VRFB electrodes and therefore, an attempt has been made to characterize the transport processes parameters in the electrodes.

Selecting appropriate electrodes is critical to the optimization of VRFBs. The electrodes provide the active sites for the reaction to occur. Their structure defines the electrical conductivity as well as describe the electrolyte flow, thereby impacting both the activation overpotential and the concentration overpotential [8] and thus influencing the mass transport overpotential. According to Minke et al. [8], a good electrode for VRFB application should have high electrical conductivity, high specific surface area, and high chemical stability. This makes carbon felts suitable for the electrodes [9].

In the selection of electrodes, four goals need to be fulfilled:

- 1 The maximum electrochemically active surface area should be

* Corresponding author.

E-mail address: rupak.banerjee@kit.edu (R. Banerjee).

<https://doi.org/10.1016/j.est.2018.11.014>

Received 14 September 2018; Received in revised form 12 November 2018; Accepted 13 November 2018

2352-152X/ © 2018 The Authors. Published by Elsevier Ltd. This is an open access article under the CC BY-NC-ND license (<http://creativecommons.org/licenses/by-nc-nd/4.0/>).

- available, addressing the need for larger surface area per projected area.
- The pressure drop of the fluid passing through the electrode must be low, in order to minimize the parasitic loss arising from pumping power.
 - The saturation of the electrode by the electrolyte must be maximized such that the largest possible electrochemically active area is maintained providing the largest area for the reaction to occur and maintaining low reaction rates.
 - The effective rate of diffusion of electroactive ions (Vanadium ions in this case) should be maximized in order to ensure the reactants reach the electroactive sites rapidly and the products are removed efficiently.

Significant work has been done in developing and modifying carbon felt electrodes to improve the performance of VRFBs [9–12]. Several authors have investigated the possibility of using electrospun carbon nanofibers as electrode materials for VRFBs [13–17]. However, more needs to be done in characterizing the different transport mechanisms in these electrodes for better comparison of the electrodes. Kim and Park [18] experimentally measured the effect of temperature on transport parameters such as activation overpotential and ohmic overpotential, demonstrating that performance of the VRFBs improves with temperature up to a temperature of 318 K (44.85 °C). Zhang et al. [19] also demonstrated an improvement in performance and voltage efficiency up to a temperature of 55 °C, although a decrease in columbic efficiency was observed with increasing temperature over the same range. Wang et al. [20] investigated the impact of compression on the transport parameters, and showed a decrease of permeability with an increase in compression of the felt. The compression also increased the intrusion of the felt into the flow channels, resulting in an increased pressure drop. This effect of compression on intrusion and pressure drop has also been shown in earlier investigations for PEM fuel cells [21]. Kok et al. [22,23] used X-ray computed tomography to investigate structural parameters of electrodes for VRFBs. They demonstrated that their electrospun carbon nanofiber electrodes manufactured in-house had fairly uniform fiber diameters of about 2 μm diameters, while local porosity showed significant heterogeneity in the through-plane direction varying between 84% and 96%.

Schweiss et al. [24] used in situ electrochemical measurements to identify the factors which impact the performance of the flow battery cell the most. They demonstrated that surface oxygen groups on the carbon fibers are beneficial to the negative electrode (V^{2+}/V^{3+}), but has no significant impact on the positive electrode (V^{4+}/V^{5+}). On the positive electrode, the electronic conductivity of the felts was shown to be the most important criterion. Eifert et al. [25] also demonstrated that the high hydrogen gas evolution at the positive electrode could result in multi-phase flow.

The electrolyte flow in VRFBs can be classified into flow-through type and flow-by type based on the bipolar plates used in the VRFB cell [26–28]. Conventionally, most investigations have focussed on the flow-by type of flow fields for their similarity with fuel cells as well as small pressure drops [28–30]. One of the main drawbacks of flow-through type flow fields involve high pressure drops due to the high resistance of flow through a porous media compared to that through a channel. However, Houser et al. [26] demonstrated that the parasitic power loss due to the increase in pressure drop can be countered by optimizing operating conditions and flow rates. The higher electrochemical surface area available for the reaction when operating as a flow-through electrode, allows for higher current densities to be achieved even with lower flow rates. The benefits of a flow-through design is observed most clearly at the low flow rates where they result in higher performance, while the flow-by design shows a higher performance at higher flow rates [28]. In order to improve these predictions of pressure drop and parasitic losses, it is important to understand the transport properties of different materials.

Pore network modeling is a powerful modeling approach that simplifies the computation of flow properties through a porous medium by treating the pore space as a network of pores connected by throats. Although the technique was first developed for low porosity materials [31,32], the modeling technique has been shown to work well for high porosity materials [33,34]. They have been successfully used to model the transport of reactant gases and product water through the gas diffusion layers of PEM fuel cells [35–39], which are also carbon fiber based porous medium with a porosity greater than 80%. Several authors have used the modeling approach of pore network modeling to predict the saturation, permeability and other transport properties through high porosity materials [34–36,40–42].

In this work, three commercially available carbon felt electrodes from SGL® Carbon and one carbon felt electrode from TOYOBO® have been investigated for their different transport properties. These have been used to demonstrate the utility of our modeling approach in identifying the transport properties and in comparing materials for their transport properties. These four materials have been compared for both diffusive transport as well as pressure driven transport.

2. Methodology

This section describes the samples investigated and their basic properties, as well as the characterization techniques used in this work. Pore network modeling is used to investigate the transport properties of the carbon felt electrodes.

2.1. Description of samples

Three samples of carbon felt electrodes from SIGRACELL battery electrodes (a division of SGL Carbon, Meitingen, Germany), and one sample of carbon felt electrode from TOYOBO (Osaka, Japan) were investigated in this study. Details of the carbon felt electrodes are provided in Table 1, which are obtained from the manufacturer's specification sheets.

SGL KFD 2.5 is the thinnest of the three SGL samples with a thickness of 2.5 mm. The thickness of the samples increases progressively to 4.6 mm for GFD 4.6 and 6 mm for GFA 6. The samples have their thickness included in their code name, making it easier to recall. The XF-30 A electrode from TOYOBO has a thickness of 4.3 mm, which makes it best comparable to GFD 4.6 in terms of thickness. Each of the samples was investigated in their pristine form, and after activation. Activation involved baking the sample at a temperature of 400 °C for a 25-hour period in ambient air. The activation has been recommended in the literature [11,43] and has been shown to improve the performance of the electrode during operation of the VRFBs. The impact of activation on the samples will be discussed in the results.

2.2. Contact angle measurement

The surface wettability of the carbon electrodes was measured through the analysis of contact angles. The static contact angle was measured for each of the samples using a goniometer (KRUSS GmbH, Germany) coupled with a DSA 10 Mk2 (KRUSS GmbH, Germany) drop

Table 1

Summary of properties for the samples studied in this investigation (in non-activated state).

Properties	KFD 2.5	GFD 4.6	GFA 6	XF-30A
Thickness ^a (mm)	2.5	4.6	6	4.3
Areal Weight ^a (g/m ²)	250	465	500	330
Open Porosity ^a (%)	> 90	94	95	–
Contact Angle ^b (Pristine)	138° ± 6°	143° ± 4°	137° ± 5°	135° ± 5°

^a from manufacturer specifications.

^b measured.

shape analysis system. The drop shape and the contact angle were extracted using the sessile drop model. The contact angle for each of the pristine samples is shown in Table 1.

The measurements were repeated after the samples were activated as described above. The materials became hydrophilic after activation and the droplet was wicked into the porous structure as soon as it interacted with the internal pores. As the water droplet was wicked in, no contact angle could be measured, and a hydrophilic contact angle of 40° is assumed for all the activated samples. This is in agreement with Gopalan and Kandlikar [44], who demonstrated that the surface roughness of porous materials makes it difficult to measure the contact angle on their surface.

2.3. X-Ray CT

The carbon electrodes were investigated by imaging their structure using X-ray computed tomography (X-ray CT) conducted with a Skyscan 1172 desktop device (Bruker Corp., MA, USA). A series of radiographs were captured at an energy level of 36 kV, with a source current of 222 μ A. The images were captured after rotating the sample sequentially by 0.2° at each step, and the spatial resolution obtained was 2.07 μ m/pixel. These images were then reconstructed into a grayscale three-dimensional image using NRECON® software (Bruker Corp.). The imaging and the analysis have been used in a manner consistent with the literature [40,45,46].

The output from the reconstruction software was a greyscale three-dimensional image. A threshold is applied to this to identify the solid regions of the porous material and thereby isolate the pore space. The threshold is applied in the image manipulation software FIJI (ImageJ) [47]. Additionally, a median filter is used to remove any remaining noise after the threshold process. The final result is a binary image where 0s are used to represent the pore space and 1s are used to represent the solid space.

2.4. Pore space extraction

The binary image obtained from the segmentation of the X-ray CT image was then used to obtain the pore space information. This image marks all the solid regions as 1s while all the pore regions are marked as 0s. An algorithm developed by Gostick et al. [48] was utilized to extract the pore space of the carbon felt electrode in the form of pores and throats, to be modeled using the pore networking modeling approach. The pore space is extracted using a watershed segmentation which isolates the void space based on the distance from the nearest solid (fiber) region. The algorithm is implemented using a Python code. Fig. 1 demonstrates the definitions of pore and throat regions as has been defined for the pore network modeling approach used here [35,49–52]. The pore network modeling performed in this work is done using the open source pore network modeling framework, OpenPNM [49,50]. The basis of pore network modeling has been well described by Hinebaugh et al. [33].

OpenPNM has previously been used to investigate high porosity porous media such as gas diffusion layer for PEM fuel cells [35–39]. Gostick et al. [34,37,49] validated the model for such porous materials. The development of the OpenPNM framework has been done to encourage other researchers to use it as a tool to investigate a variety of materials [49,50]. In this work, OpenPNM has been utilized as it has been successfully used with similar materials and the model is well validated.

Fig. 2 presents the illustration of the materials investigated in this study at the different stages of their processing. Illustrations are provided for the material KFD 2.5 for representation. The other materials have been processed in the same manner. Fig. 2(a) shows the structure of the felt electrode as obtained from the X-ray CT after it has been segmented into the solid and void regions. Fig. 2(b) shows only the pore network that is used for the simulation.

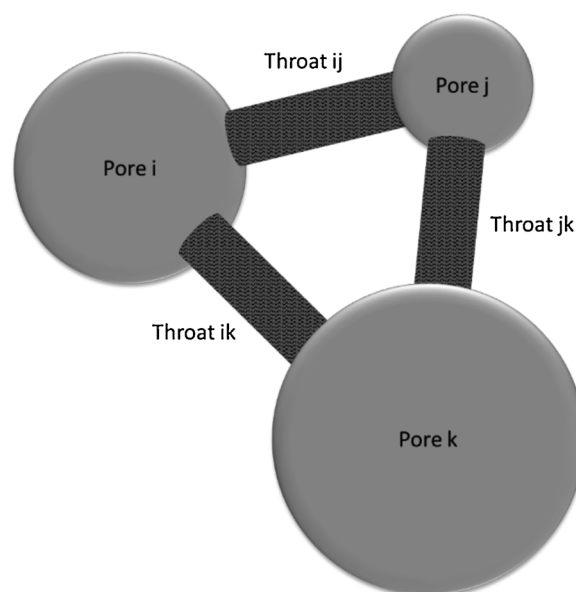


Fig. 1. Representation of pore and throat configuration for calculation of pore scale properties in the pore space.

2.5. Permeability

The permeability of the porous media is calculated by applying a pressure boundary condition on the two opposite faces of the network and calculating the flux of fluid flowing through the network of pores and throats. A pressure difference of 101,325 Pa (1 atm) is applied across the opposite faces of the pore network. This is then used to calculate the permeability using Darcy's law [53–55], as shown in Eq. (3).

$$K = \frac{Q}{A} \frac{\mu L}{\Delta P} \quad (3)$$

where Q is the flow rate of fluid passing through the porous media, μ is the viscosity of the fluid, L is the distance the fluid travels through the porous medium (thickness of sample in this case), A is the area of cross-section, and ΔP is the pressure difference driving the fluid flow.

As seen from Eq. (3), the permeability of the porous media is impacted by the pore space (porosity and tortuosity), and the surface interaction between the electrode and the electrolyte. Permeability is a property of the porous medium in response to pressure driven flow, and therefore the viscosity of the fluid also has an impact.

2.6. Diffusivity

The diffusivity of the porous medium is calculated using the Fickian diffusion model. This is applicable as the pores in this material have a diameter larger than 1 μ m, and Knudsen diffusion does not have a significant contribution to the overall transport process [56,57]. Additionally, as the electrode is flooded with electrolyte during operation, the mean free path for molecules is very small, leading to insignificant contribution of Knudsen diffusion.

In calculating the Fickian diffusion across the porous medium, a concentration boundary condition is set at the two opposite faces of the material and a linear transport assumption is used to calculate the diffusive flux. The effective diffusion coefficient is calculated using Fick's law as shown below:

$$D = \frac{L \times N}{A \times (C_{in} - C_{out})} \quad (4)$$

where D is the diffusion coefficient, L is the path length (thickness of material), N is the flux of diffusive component, A is the cross-sectional

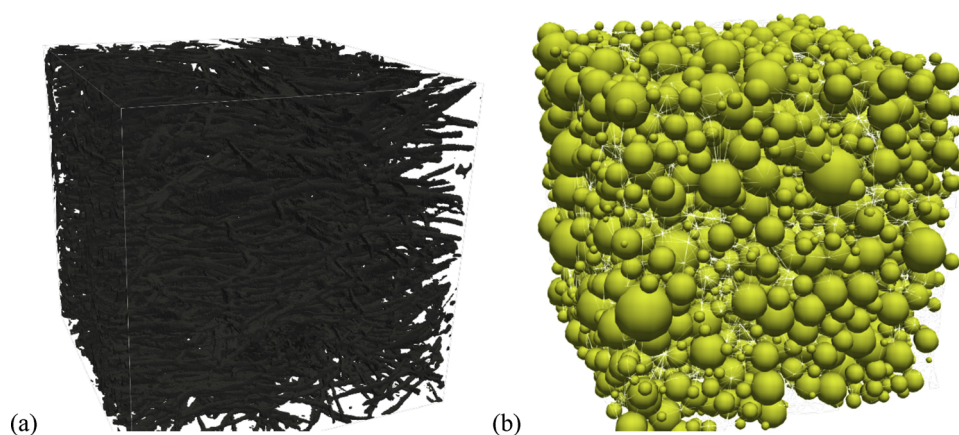


Fig. 2. Pore network extraction of a sample GFA 6. (a) Three-dimensional image of X-ray CT of sample. (b) Spherical representation of the pore network as obtained for the sample.

area, and C_{in} and C_{out} are the concentrations of the inlet and outlet faces, respectively. This model of calculating effective diffusion coefficient has been used in the literature [58] and utilizes the inbuilt functionality of OpenPNM [50].

From Eq. (4), it is observed that the flow is concentration driven and is dependent only on the physical pore space. The diffusion mechanism is not impacted by the fluid properties (such as viscosity) and the material surface properties.

In the presence of the electrolyte, the diffusion coefficient is modified such that saturated pores contribute to the diffusion in accordance with the effective diffusion coefficient of the saturating fluid, while unsaturated pores are assigned the effective diffusion coefficient of the ambient fluid. This is utilized to investigate the changes in diffusivity of active $V^{2+}/V^{3+}/V^{4+}/V^{5+}$ ions in the electrolyte with changes in electrolyte saturation. This diffusivity in the presence of two-phase interaction, is presented as the relative diffusivity. The relative diffusivity is calculated as shown in Eq. (5).

$$D_{relative} = \frac{D_{two-phase}}{D_{single-phase}} \quad (5)$$

2.7. Imbibition

Pressure drop has been shown to be a key concern in the flow-through type electrode design. In order to better characterize the pressure drop, the imbibition curve is calculated which demonstrates the pressures required to invade the porous medium to different levels of saturation. A fully saturated porous media results in the highest active surface area available for the reaction to take place. The pressure is increased until a fully saturated porous media is obtained. The rate of change of saturation with respect to the capillary pressure applied to invade the pore space gives us an insight into the ease of transport in the pore space. The imbibition plot also provides information about the pores that may never get filled in a real application due to a large capillary pressure jump.

2.8. Invasion percolation

To track the invasion of the electrolyte into the porous layers, an invasion percolation algorithm was utilized. The invasion percolation algorithm used was presented in detail by Fazeli et al. [44] and has been built into the OpenPNM framework [50]. The process of invasion percolation follows the definition outlined by Wilkinson and Willemsen [50]. The invasion process neglects viscous forces and calculates transport by capillary forces. In simulating the invasion percolation through this porous medium, one face of the porous medium was completely saturated with the electrolyte and the transport was tracked

as the electrolyte percolates through the porous domain to reach the opposite face of the medium. When the first pore of the opposite face was invaded by the electrolyte, this point was referred to as the breakthrough point, and the saturation of the porous medium at the time of breakthrough, and the pressure required to reach breakthrough were both calculated. The point of breakthrough represents a state in which the electrolyte has a continuous path through the electrode and a flow path can be maintained. It is the lowest pressure for the electrode to be utilized with the particular electrolyte.

3. Results & discussion

In this section, the results of the evaluation of the pore structure, contact angle, and the transport properties are presented. Comparisons are drawn between the four samples studied in this investigation as well as the impact of activation of the samples on their transport properties. The impact of the transport property on the VRFB performance is also highlighted to provide context to the findings.

3.1. Pore size distribution

Fig. 3 shows the distribution of the pore diameters of the four samples investigated. They all display a similar distribution of pore diameter distributions. The pore diameters obtained from the pore network extraction have been binned into groups of $5\ \mu\text{m}$ widths and the frequency of their occurrence tallied. It is observed that no pores were found to be smaller than $10\ \mu\text{m}$ for all the samples. The modal

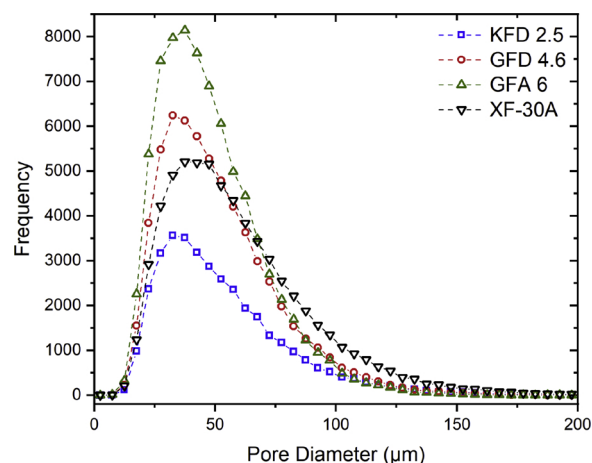


Fig. 3. Distribution of pore diameters of the four materials evaluated in this study.

pore size for these carbon felt electrodes can be observed to be between 30–40 μm for the three SGL samples, while XF-30 A demonstrated slightly higher pore sizes with the modal value observed between 35–50 μm . Beyond the modal value, the number of pores decreases with an increase in pore size with a negligible number of pores being larger than 150 μm . This trend holds true for all the carbon electrodes being investigated in this study. However, the number of pores for each of the electrodes varies significantly, with KFD 2.5 having approximately 36,000 pores, GFD 4.6 having 62,000 pores, GFA 6 having 76,000 pores, and XF-30 A having 64,000 pores, for the same cross-sectional area of investigation. This is attributed to the different thickness of each of these samples, as reported in Table 1, which provides details about each of the electrode materials. GFA 6 is the thickest sample and therefore has the most volume for the given area of investigation, resulting in the largest number of pores, while KFD 2.5 is the thinnest sample, resulting in the least volume for the given area, and the smallest number of pores.

From the distributions of pore diameters, it was observed that the three carbon felt electrodes from SGL have a similar internal structure, although their thicknesses are different. For a direct comparison of pore structure, GFD 4.6 and XF-30 A can be compared as they have similar thickness and the number of pores obtained (< 5% difference). From the distribution of pore diameters, it can be observed that the XF-30 A electrode has more pores larger than 50 μm , while GFD 4.6 has a greater number of pores below 50 μm . The impact of these differences in pore sizes will be explored in the future sections on transport properties. Larger pore sizes are usually indicative of lower resistance to fluid flow. Therefore, the pore size distribution is of interest to both single-phase and two-phase flow.

3.2. Transport properties

Mass transport occurs in the flow battery electrodes via both permeability as well as by diffusion, as discussed earlier. Table 2 shows the values of permeability and diffusivity for each of the samples along the thickness of the electrode. It can be observed that permeability along the direction of thickness decreases with an increase in the thickness of the sample. It is important to note that XF-30 A has a 70% higher permeability compared to GFD 4.6, while both have similar thicknesses. This difference in permeability is driven by the larger pores in XF-30 A, as observed in Fig. 3. The importance of the higher permeability derives from the lower pressure drop expected from the highly permeable material, thus leading to lower parasitic losses. Therefore, even under single-phase flow, the lower permeability is a desirable feature for flow-through type flow batteries, so that the parasitic pumping losses are minimized.

Single-phase diffusivity was calculated through the porous network using the Fickian Diffusion model, as described in Section 2.6. The single-phase diffusion coefficient is calculated for both air as well as for water, which is representative of the electrolyte phase. The single-phase diffusion coefficient is also calculated for comparison with other diffusion media (carbon paper) from the same manufacturer. The comparison is shown in Fig. 4, and it can be observed that the single-phase diffusion coefficient is in the same range as that for the carbon paper

Table 2

Permeability and single-phase effective diffusion coefficient values calculated for the four materials.

Material	Single Phase Diffusion Coefficient (m^2/s)		Permeability (Darcy)
	Air	Water	
KFD 2.5	9.02E-06	4.36E-10	15.58
GFD 4.6	8.23E-06	3.98E-10	10.69
GFA 6	7.47E-06	3.62E-10	7.32
XF - 30A	8.74E-06	4.23E-10	17.49

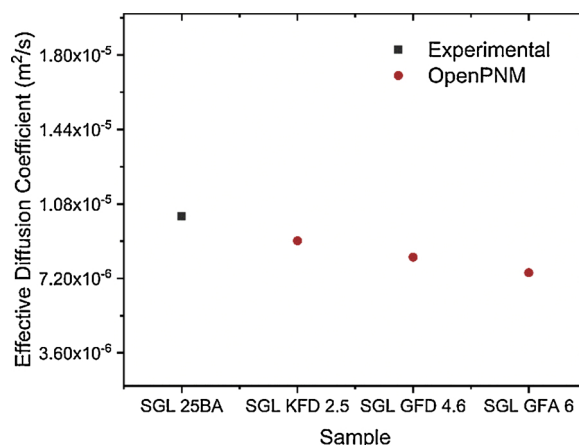


Fig. 4. Comparing single phase diffusion coefficient of SGL materials. Values calculated with OpenPNM are in the same range as experimentally measured by LaManna and Kandlikar [59].

materials of much lower thickness. However, it was also observed that the diffusion coefficient decreases very slightly with an increase in thickness, as was expected as the diffusion has to happen through a longer path of diffusive medium. For XF-30 A, the single-phase diffusion coefficient was found to be slightly higher than GFD 4.6. This is expected to lead to an improvement in mass transport overpotentials and therefore an improvement in overall performance. A higher single-phase diffusion coefficient is desirable in order to maintain a uniform concentration distribution at high utilization rates, as well as providing a high rate of removal for the product ions. In both flow-through and flow-by type configurations for flow batteries, a higher single-phase diffusion coefficient is desirable.

3.3. Electrolyte invasion into electrode

Fig. 5 shows the imbibition curves for the four materials in the non-activated state (contact angle of 140°). After activation, the materials become hydrophilic and therefore water can invade into the pores with greater ease. It was observed from the figures that the saturation undergoes a logarithmic increase with an increase in pressure. The saturation increases rapidly from a saturation of close to zero to a saturation of 0.1 for a small increase in pressure. For the saturation to increase beyond 0.9, the pressure increase is much more significant. Table 3 shows the pressure required to achieve set values of saturation. From the table, it is observed that the pressure increases are linear

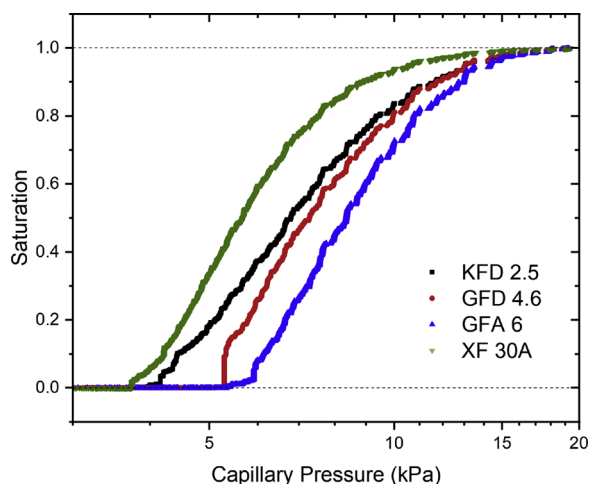


Fig. 5. Imbibition curves for the four materials. Contact angle of 140° considered, assuming non-activated samples.

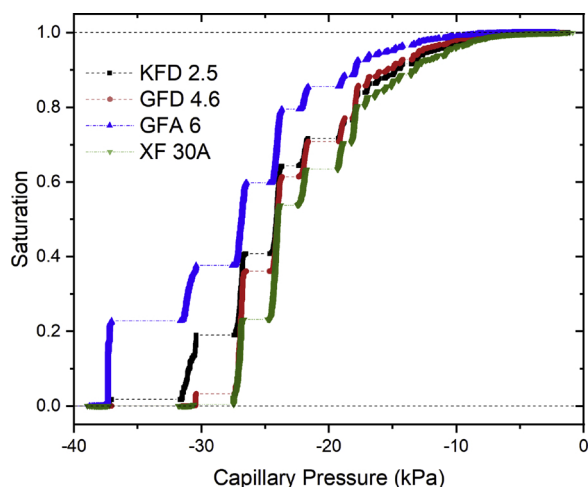


Fig. 6. Drainage curves for the four materials. Contact angle of 40° considered, assuming activated samples.

between the saturation range of 0.1 to 0.9. Above a saturation of 0.95, it is increasingly difficult for the fluid to access the final pores, as these are the smallest pores with the highest entry capillary pressures. There is an increase of 43.87 kPa of pressure for a saturation increase from 0.95 to 1.0 in the case of KFD 2.5, while for GFD 4.6 the pressure increase is 43.86 kPa, for GFA 6 the pressure increase is 42.58 kPa, and for XF-30 A the pressure increases by 46.62 kPa. This jump in pressure for the final 5% saturation indicates that the small pores require the extra pressure to be filled in, and it might be beneficial to operate the VRFBs with a saturation of 90 to 95%, thus taking advantage of the lower pressure gradient. This could result in lower parasitic losses and therefore overall higher efficiency. While the three SGL electrodes share the same porous structure, XF-30 A has larger pores. This manifests itself in the electrolyte invasion behavior and was observed as XF-30 A consistently reached higher saturation for the same capillary pressure, as larger pores fill first.

Understanding the invasion pressure is important in the case of flow batteries, even though the batteries are operated in single-phase conditions as the pressure used to saturate the electrode at start-up can have a direct impact on the saturation. This allows us to predict the pressure required to achieve high levels of saturation. A partially saturated electrode at startup will remain partially saturated throughout the operation, and therefore reduce the surface area available for electrode – electrolyte interactions. Thus, the saturation is an important criterion to be achieved if the maximum electrode surface is to be utilized even in single-phase flow condition.

Fig. 6 shows the imbibition curve for the same materials in the activated state. A contact angle of 40° is assumed for these materials in the activated state, as discussed in Section 2.2. In Fig. 6, the y-axis shows the saturation and the x-axis shows the pressure required for the electrolyte to be invaded into the electrode. It was observed that the capillary pressure is negative for the hydrophilic material, as the

material is a wicking material and the electrolyte is wicked into the electrode, creating a negative pressure. This is consistent with results reported in the literature with hydrophilic samples [60]. In contrast to the results for the non-activated state shown in Fig. 6, it can be observed from Fig. 7 that the saturation increase occurs in a step-wise manner. The step-wise growth in saturation indicates that different sets of pores become available to the electrolyte at increasing pressure and once the set of pores become available, they are immediately filled, resulting in a sudden jump in the saturation. These individual sets of pores are separated by their entry pressures.

Table 3 shows the values of properties identified as part of the invasion process of the electrolyte into the electrode. The breakthrough pressure represents the pressure required to get the first connected pathway from one side of the electrode to the other. This would allow the fluid to flow through continuously through the electrode. The breakthrough saturation is the saturation of the electrode at the time of the breakthrough. It is apparent from the data that the saturation remains quite low at the time of the breakthrough and therefore cannot be used as the saturated condition of the electrode. Also shown in Table 3 is the capillary pressure required to get the saturation to certain important levels.

3.4. Invasion patterns

Fig. 7 shows the invasion pattern of the electrolyte as it invades into the electrode material. Fig. 7(a) and (b) show the invasion patterns for the sample of KFD 2.5 in the non-activated and activated states, at the time of breakthrough. As seen in Table 3, the saturation of the electrode in the non-activated state is much lower than when the electrode is activated. This is also evident from the invasion patterns. The gradient of color shows the order in which the pores are invaded. No clear trend was observed in the order of pore invasion for this electrode.

Fig. 7(c) and (d) illustrate the invasion patterns for GFD 4.6 in the non-activated and activated states, respectively. From Table 3, it is observed that the saturation of the non-activated electrode is higher than the saturation of the activated electrode. This is not in agreement with the trends observed in the KFD 2.5 electrode. However, if the order in which the pores are filled is observed, it can be seen that in the hydrophilic case, the pores are primarily filled in a single direction (from left to right), whereas the pores are filled in a less directional manner in the hydrophobic (non-activated) case. Fig. 7(e) and (f) show the invasion patterns for GFA 6 electrode in the non-activated and activated states respectively. The same trends as GFD 4.6 electrodes are observed. The saturation of the non-activated GFA 6 electrode is higher at breakthrough compared to the activated electrode. Additionally, the directional nature of invasion as seen in GFD 4.6 is also observed in GFA 6.

Fig. 7(g) and (h) present the invasion patterns for XF-30 A in the non-activated and activated states, respectively. From Table 3, it was known that the breakthrough saturation was lower in the non-activated state. This is reinforced in the invasion patterns. Additionally, there is again a directional component to the order in which pores were filled, similar to the observations for GFD 4.6 and GFA 6. This indicates that

Table 3
Breakthrough saturation and capillary pressure at important stages of electrolyte invasion.

	KFD 2.5		GFD 4.6		GFA 6		XF 30A	
	Non Activated	Activated						
Breakthrough Saturation	0.157	0.276	0.220	0.174	0.311	0.236	0.095	0.105
Capillary Pressure (kPa)								
At Breakthrough	4.86	-26.99	5.86	-27.00	5.77	-31.43	4.22	-27.06
At 50% saturation	6.79	-24.13	7.28	-24.06	8.35	-26.86	5.67	-24.02
At 80% saturation	9.36	-17.93	9.96	-17.95	10.75	-22.15	7.53	-17.78
At 90% saturation	11.69	-14.80	11.73	-15.44	12.96	-17.96	8.86	-13.40
At 100% saturation	56.93	-1.24	56.91	-1.62	56.91	-1.95	57.21	-0.88

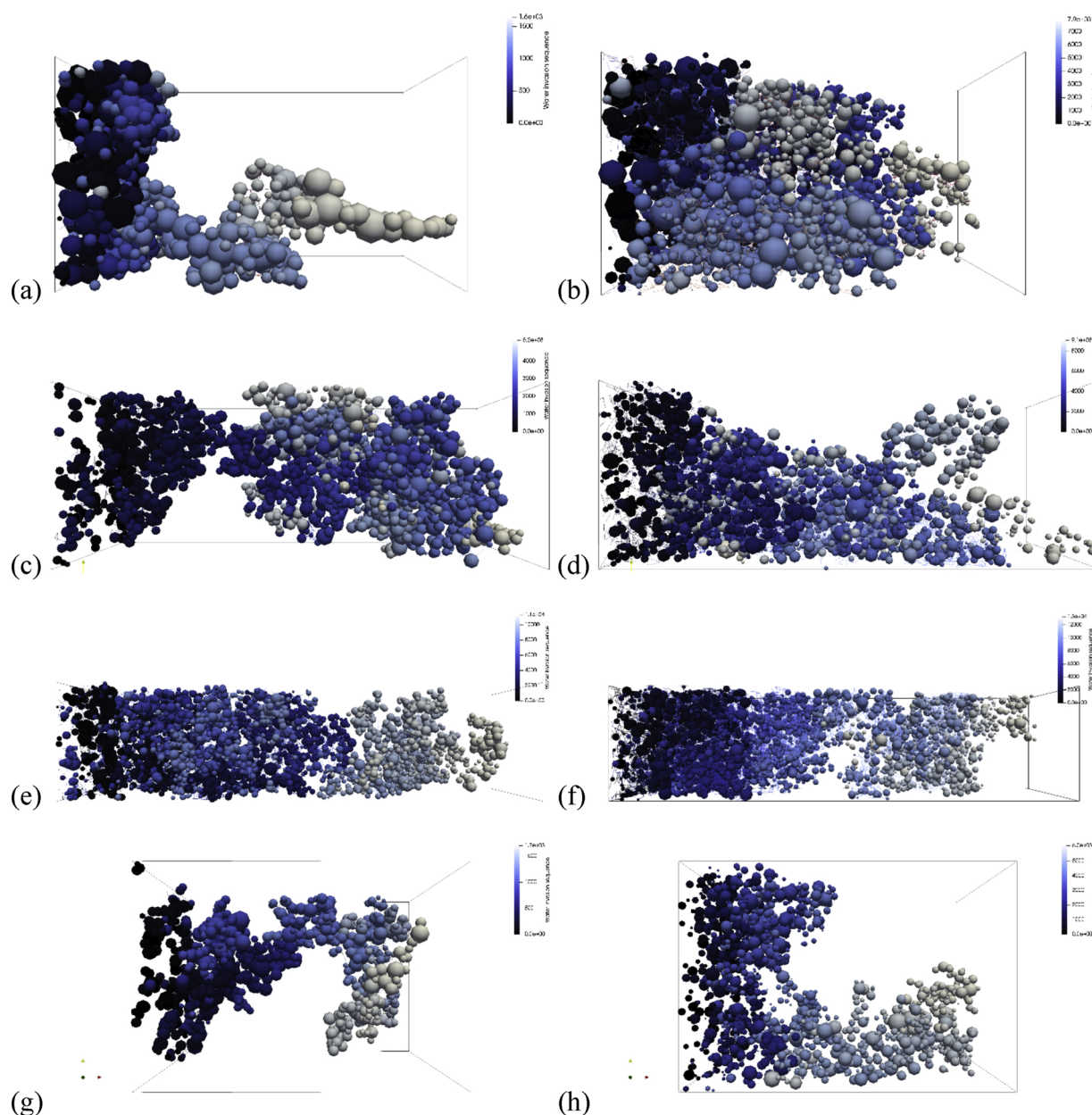


Fig. 7. Invasion patterns observed for the electrolyte invasion into the electrodes for the four materials under both non-activated and activated states: (a) KFD 2.5 Non Activated (b) KFD 2.5 Activated (c) GFD 4.6 Non Activated (d) GFD 4.6 Activated (e) GFA 6 Non Activated (f) GFA 6 Activated (g) XF-30 A Non Activated (h) XF-30 A Activated.

the directional component of invasion occurs only with thicker samples. The difference in the saturation and invasion trends observed between KFD 2.5 and the three other electrodes (GFD 4.6, GFA 6, and XF-30 A) can be estimated to be due to the smaller thickness of the KFD 2.5 electrode which results in fewer pores required to be filled before the breakthrough state is reached.

3.5. Relative diffusivity

Fig. 8 shows the relative diffusivity of the electrolyte with changes in saturation of electrolyte in the porous electrode. The relative diffusivity increases with an increase in saturation of the electrolyte, although no significant diffusivity is observed below a saturation of 0.3. At the low saturation levels, the electrolyte does not have a continuous path across the whole of the electrode, resulting in the negligible levels of relative diffusivity. All the SGL samples of felt electrodes in both the

activated and non-activated states showed the same trend for relative diffusivity. This demonstrates that the relative diffusivity is dependent on the internal pore structure of the electrode, as the internal structure is the same for all three of these electrodes, as shown in Section 3.1. The relative diffusivity of the electrolyte is independent of the thickness of the electrodes or its activation state. The relative diffusivity of the electrolyte demonstrates an exponential increase reaching a value of unity, i.e. equal to the single-phase diffusivity, which is expected as single-phase diffusion state is reached when the electrode is fully saturated with the electrolyte. The flow battery is unable to function at saturations below 0.3 where the active charge-carrying ions can neither maintain a continuous diffusive path to the reaction sites and the product ions cannot be effectively removed. This result demonstrates that a lower threshold exists for the saturation of the electrode, below which the VRFB is unable to maintain continuous operation.

From the figure, it is also evident that XF-30 A has a small difference

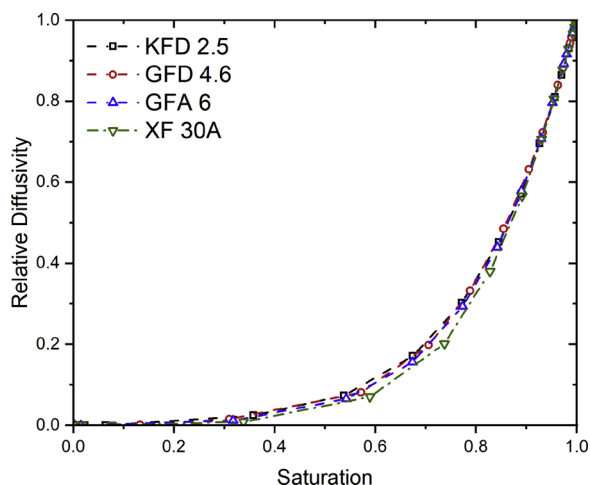


Fig. 8. Relative diffusivity as a function of electrolyte saturation in the porous electrode.

in the relative diffusivity resulting from the small difference in pore structure observed in Section 3.1. In the saturation range of 0.4 to 0.9, XF-30 A shows a slightly lower relative diffusivity compared to the SGL felt electrodes which have identical pore size distributions. From Section 3.1 we know that XF-30 A has more of the larger pores. As the pores are filled, if the larger pores are filled, they occupy a larger volume and therefore the saturation increases, although that might not result in more connected pathways. The distribution of these connected pathways provides a good measure for the relative diffusivity of the electrolyte through the electrode.

4. Conclusions

In this work, three commercially available carbon felt electrode materials from SGL Carbon, and one carbon felt electrode from TOYOBO Carbon have been investigated for their different transport properties. As part of this work, the single-phase diffusion coefficient, single-phase permeability, relative diffusivity, and the imbibition trends are obtained for each of the three materials. From these investigations, the following conclusions can be drawn:

- All of the studied materials have similar internal pore structures, although the thickness of the samples is different for the three SGL materials, and the electrode from TOYOBO has larger pores.
- The single-phase permeability and the diffusion coefficient decreases with the increase in thickness of the sample.
- The three materials have similar imbibition curves representing the pressure required for the invasion of the electrode by the electrolyte. The entry pressure into the sample increases at the lowest saturation levels, with an increase in thickness. Changing the wettability has a strong impact on the imbibition curve.
- Relative diffusivity is not impacted by the thickness of the samples or the activation state, but rather is a function of the internal pore structure of the materials.
- Electrode saturation lower than 30% is unable to sustain continuous operation of a VRFB due to the low relative diffusivity which hinders the supply and removal of active charge-carrying ions to and from the reaction sites.

This work also highlights a set of pre-existing tools which can be utilized to understand the transport properties of VRFB electrodes. These tools can be used to compare materials of different pore structure and gain a better understanding of the requirements for an improved Vanadium redox flow battery.

Acknowledgements

The authors acknowledge the “Impuls- und Vernetzungsfonds der Helmholtz Gesellschaft” for the financial support (Young Investigator Group project VH-NG-616). The authors thank SGL group for providing the SGL samples used in this investigation. The authors would also like to thank the Zentrum für Sonnenenergie- und Wasserstoff-Forschung Baden-Württemberg (ZSW) for the use of their microcomputed tomography facilities utilized in this investigation. This work contributes to the research performed at CELEST (Center for Electrochemical Energy Storage Ulm-Karlsruhe).

References

- [1] N.R. Council, The National Academies Summit on America's Energy Future: Summary of a Meeting, (2008), <https://doi.org/10.17226/12450>.
- [2] A.Z. Weber, M.M. Mench, J.P. Meyers, P.N. Ross, J.T. Gostick, Q. Liu, Redox flow batteries: a review, *J. Appl. Electrochem.* 41 (2011) 1137, <https://doi.org/10.1007/s10800-011-0348-2>.
- [3] X.L. Zhou, T.S. Zhao, L. An, Y.K. Zeng, L. Wei, Critical transport issues for improving the performance of aqueous redox flow batteries, *J. Power Sour.* 339 (2017) 1–12, <https://doi.org/10.1016/j.jpowsour.2016.11.040>.
- [4] M. Skyllas-Kazacos, M.H. Chakrabarti, S.A. Hajimolana, F.S. Mjalli, M. Saleem, Progress in flow battery research and development, *J. Electrochem. Soc.* 158 (2011) R55–79, <https://doi.org/10.1149/1.3599565>.
- [5] R.M. Darling, K.G. Gallagher, J.A. Kowalski, S. Ha, F.R. Brushett, Pathways to low-cost electrochemical energy storage: a comparison of aqueous and nonaqueous flow batteries, *Energy Environ. Sci.* 7 (2014) 3459–3477, <https://doi.org/10.1039/C4EE02158D>.
- [6] A. Parasuraman, T.M. Lim, C. Menictas, M. Skyllas-Kazacos, Review of material research and development for vanadium redox flow battery applications, *Electrochim. Acta* 101 (2013) 27–40, <https://doi.org/10.1016/j.electacta.2012.09.067>.
- [7] P. Alotto, M. Guarnieri, F. Moro, Redox flow batteries for the storage of renewable energy: a review, *Renew. Sustain. Energy Rev.* 29 (2014) 325–335, <https://doi.org/10.1016/j.rser.2013.08.001>.
- [8] C. Minke, U. Kunz, T. Turek, Carbon felt and carbon fiber - A techno-economic assessment of felt electrodes for redox flow battery applications, *J. Power Sour.* 342 (2017) 116–124, <https://doi.org/10.1016/j.jpowsour.2016.12.039>.
- [9] J.-Z. Chen, W.-Y. Liao, W.-Y. Hsieh, C.-C. Hsu, Y.-S. Chen, All-vanadium redox flow batteries with graphite felt electrodes treated by atmospheric pressure plasma jets, *J. Power Sour.* 274 (2015) 894–898, <https://doi.org/10.1016/j.jpowsour.2014.10.097>.
- [10] G. Wei, C. Jia, J. Liu, C. Yan, Carbon felt supported carbon nanotubes catalysts composite electrode for vanadium redox flow battery application, *J. Power Sour.* 220 (2012) 185–192, <https://doi.org/10.1016/j.jpowsour.2012.07.081>.
- [11] K.J. Kim, Y.-J. Kim, J.-H. Kim, M.-S. Park, The effects of surface modification on carbon felt electrodes for use in vanadium redox flow batteries, *Mater. Chem. Phys.* 131 (2011) 547–553, <https://doi.org/10.1016/j.matchemphys.2011.10.022>.
- [12] T.J. Davies, J.J. Tummino, High-performance vanadium redox flow batteries with graphite felt electrodes, *C* 4 (2018) 8, <https://doi.org/10.3390/c4010008>.
- [13] S.P. Liu, M. Kok, J.T. Gostick, Fabrication and characterization of electrospun electrodes for flow battery electrodes, *ECS Trans.* 75 (2017) 15–25, <https://doi.org/10.1149/07518.0015sect>.
- [14] S. Liu, M. Kok, Y. Kim, J.L. Barton, F.R. Brushett, J. Gostick, Evaluation of electrospun fibrous mats targeted for use as flow battery electrodes, *J. Electrochem. Soc.* 164 (2017) A2038–48, <https://doi.org/10.1149/2.1301709jes>.
- [15] Fetyan Abdulmonem, Derr Igor, Kayarkatte Manoj Krishna, Langner Joachim, Bernsmeier Denis, Kraehnert Ralph, et al., Electrospun carbon nanofibers as alternative electrode materials for vanadium redox flow batteries, *ChemElectroChem* 2 (2015) 2055–2060, <https://doi.org/10.1002/celec.201500284>.
- [16] A. Di Blasi, C. Busacca, O. Di Blasia, N. Briguglio, G. Squadrito, V. Antonucci, Synthesis of flexible electrodes based on electrospun carbon nanofibers with Mn3O4 nanoparticles for vanadium redox flow battery application, *Appl. Energy* 190 (2017) 165–171, <https://doi.org/10.1016/j.apenergy.2016.12.129>.
- [17] G. Wei, X. Fan, J. Liu, C. Yan, Electrospun carbon nanofibers/electrocatalyst hybrids as asymmetric electrodes for vanadium redox flow battery, *J. Power Sour.* 281 (2015) 1–6, <https://doi.org/10.1016/j.jpowsour.2015.01.161>.
- [18] J. Kim, H. Park, Experimental analysis of discharge characteristics in vanadium redox flow battery, *Appl. Energy* 206 (2017) 451–457, <https://doi.org/10.1016/j.apenergy.2017.08.218>.
- [19] C. Zhang, T.S. Zhao, Q. Xu, L. An, G. Zhao, Effects of operating temperature on the performance of vanadium redox flow batteries, *Appl. Energy* 155 (2015) 349–353, <https://doi.org/10.1016/j.apenergy.2015.06.002>.
- [20] Q. Wang, Z.G. Qu, Z.Y. Jiang, W.W. Yang, Experimental study on the performance of a vanadium redox flow battery with non-uniformly compressed carbon felt electrode, *Appl. Energy* 213 (2018) 293–305, <https://doi.org/10.1016/j.apenergy.2018.01.047>.
- [21] S.G. Kandlikar, Z. Lu, T.Y. Lin, D. Cooke, M. Daino, Uneven gas diffusion layer intrusion in gas channel arrays of proton exchange membrane fuel cell and its effects on flow distribution, *J. Power Sour.* 194 (2009) 328–337, <https://doi.org/10.1016/j.jpowsour.2009.01.011>.

- 1016/j.jpowsour.2009.05.019.
- [22] M.D.R. Kok, R. Jervis, P.R. Shearing, J.T. Gostick, Fluid transport properties from 3D tomographic images of electrospun carbon electrodes for flow batteries, *ECS Trans.* 77 (2017) 129–143, <https://doi.org/10.1149/07711.0129ecst>.
- [23] M.D.R. Kok, R. Jervis, D. Brett, P.R. Shearing, J.T. Gostick, Insights into the effect of structural heterogeneity in carbonized electrospun fibrous mats for flow battery electrodes by X-Ray tomography, *Small* (2018), <https://doi.org/10.1002/smll.201703616> n.d./n/a-n/a.
- [24] R. Schweiss, C. Meiser, F.W.T. Goh, Steady-state measurements of vanadium redox-flow batteries to study particular influences of carbon felt properties, *ChemElectroChem* 4 (2017) 1969–1974, <https://doi.org/10.1002/celec.201700280>.
- [25] L. Eifert, Z. Jusys, R. Banerjee, R.J. Behm, R. Zeis, Differential electrochemical mass spectrometry of carbon felt electrodes for vanadium redox flow batteries, *ACS Appl. Mater. Interfaces* (2018), <https://doi.org/10.1021/acsaem.8b01550>.
- [26] J. Houser, A. Pezeshki, J.T. Clement, D. Aaron, M.M. Mench, Architecture for improved mass transport and system performance in redox flow batteries, *J. Power Sour.* 351 (2017) 96–105, <https://doi.org/10.1016/j.jpowsour.2017.03.083>.
- [27] Q. Xu, T.S. Zhao, P.K. Leung, Numerical investigations of flow field designs for vanadium redox flow batteries, *Appl. Energy* 105 (2013) 47–56, <https://doi.org/10.1016/j.apenergy.2012.12.041>.
- [28] Q. Xu, T.S. Zhao, C. Zhang, Performance of a vanadium redox flow battery with and without flow fields, *Electrochim. Acta* 142 (2014) 61–67, <https://doi.org/10.1016/j.electacta.2014.07.059>.
- [29] S. Kumar, S. Jayanti, Effect of flow field on the performance of an all-vanadium redox flow battery, *J. Power Sour.* 307 (2016) 782–787, <https://doi.org/10.1016/j.jpowsour.2016.01.048>.
- [30] T. Jyothi Latha, S. Jayanti, Ex-situ experimental studies on serpentine flow field design for redox flow battery systems, *J. Power Sour.* 248 (2014) 140–146, <https://doi.org/10.1016/j.jpowsour.2013.09.084>.
- [31] D. Wilkinson, J.F. Willemsen, Invasion percolation: a new form of percolation theory, *J. Phys. Math Gen.* 16 (1983) 3365, <https://doi.org/10.1088/0305-4470/16/14/028>.
- [32] B. Berkowitz, R.P. Ewing, Percolation theory and network modeling applications in soil physics, *Surv. Geophys.* 19 (1998) 23–72, <https://doi.org/10.1023/A:1006590500229>.
- [33] J. Hinebaugh, P.P. Mukherjee, A. Bazylak, Multi-scale modeling of two-phase transport in polymer electrolyte fuel cells, *Polym. Electrolyte Membr. Direct Methanol Fuel Cell Technol. Vol. 1 Fundam. Perform. Low Temp. Fuel Cells, 1st ed.*, Woodhead Publishing, 2012.
- [34] J.T. Gostick, M.A. Ioannidis, M.W. Fowler, M.D. Pritzker, Pore network modeling of fibrous gas diffusion layers for polymer electrolyte membrane fuel cells, *J. Power Sour.* 173 (2007) 277–290, <https://doi.org/10.1016/j.jpowsour.2007.04.059>.
- [35] M. Fazeli, J. Hinebaugh, A. Bazylak, Investigating inlet condition effects on PEMFC GDL liquid water transport through pore network modeling, *J. Electrochem. Soc.* 162 (2015) F661–668, <https://doi.org/10.1149/2.0191507jes>.
- [36] M. Fazeli, J. Hinebaugh, Z. Fishman, C. Tötze, W. Lehnert, I. Manke, et al., Pore network modeling to explore the effects of compression on multiphase transport in polymer electrolyte membrane fuel cell gas diffusion layers, *J. Power Sour.* 335 (2016) 162–171, <https://doi.org/10.1016/j.jpowsour.2016.10.039>.
- [37] T.G. Tranter, J.T. Gostick, A.D. Burns, W.F. Gale, Pore network modeling of compressed fuel cell components with OpenPNM, *Fuel Cells Weinh. (Weinh)* 16 (2016) 504–515, <https://doi.org/10.1002/fuce.201500168>.
- [38] M. Shahraeini, M. Hoorfar, Pore-network modeling of liquid water flow in gas diffusion layers of proton exchange membrane fuel cells, *Int. J. Hydrogen Energy* 39 (2014) 10697–10709, <https://doi.org/10.1016/j.ijhydene.2014.05.017>.
- [39] P.K. Sinha, C.-Y. Wang, Pore-network modeling of liquid water transport in gas diffusion layer of a polymer electrolyte fuel cell, *Electrochim. Acta* 52 (2007) 7936–7945, <https://doi.org/10.1016/j.electacta.2007.06.061>.
- [40] N. Bevilacqua, M.G. George, S. Galbiati, A. Bazylak, R. Zeis, Phosphoric acid invasion in high temperature PEM fuel cell gas diffusion layers, *Electrochim. Acta* 257 (2017) 89–98, <https://doi.org/10.1016/j.electacta.2017.10.054>.
- [41] S. Chevalier, M. Fazeli, F. Mack, S. Galbiati, I. Manke, A. Bazylak, et al., Role of the microporous layer in the redistribution of phosphoric acid in high temperature PEM fuel cell gas diffusion electrodes, *Electrochim. Acta* 212 (2016) 187–194, <https://doi.org/10.1016/j.electacta.2016.06.121>.
- [42] A. Wong, R. Banerjee, A. Bazylak, Tuning MPL intrusion to increase oxygen transport in dry and partially saturated polymer electrolyte membrane fuel cell gas diffusion layers, *J. Electrochem. Soc.* (In review).
- [43] Q.H. Liu, G.M. Grim, A.B. Papandrew, A. Turhan, T.A. Zawodzinski, M.M. Mench, High performance vanadium redox flow batteries with optimized electrode configuration and membrane selection, *J. Electrochem. Soc.* 159 (2012) A1246–52, <https://doi.org/10.1149/2.051208jes>.
- [44] P. Gopalan, S.G. Kandlikar, Effect of channel material on water droplet dynamics in a PEMFC gas channel, *J. Electrochem. Soc.* 160 (2013) F487–95, <https://doi.org/10.1149/2.030306jes>.
- [45] R. Banerjee, J. Hinebaugh, H. Liu, R. Yip, N. Ge, A. Bazylak, Heterogeneous porosity distributions of polymer electrolyte membrane fuel cell gas diffusion layer materials with rib-channel compression, *Int. J. Hydrogen Energy* 41 (2016) 14885–14896, <https://doi.org/10.1016/j.ijhydene.2016.06.147>.
- [46] R. Banerjee, S. Chevalier, H. Liu, J. Lee, R. Yip, K. Han, et al., A comparison of felt-type and paper-type gas diffusion layers for polymer electrolyte membrane fuel cell applications using X-Ray techniques, *J. Electrochem. Energy Convers. Storage* 15 (2018), <https://doi.org/10.1115/1.4037766> 011002.
- [47] J. Schindelin, I. Arganda-Carreras, E. Frise, V. Kaynig, M. Longair, T. Pietzsch, et al., Fiji: an open-source platform for biological-image analysis, *Nat. Methods* 9 (2012) 676–682, <https://doi.org/10.1038/nmeth.2019>.
- [48] J.T. Gostick, Versatile and efficient pore network extraction method using marker-based watershed segmentation, *Phys. Rev. E* 96 (2017), <https://doi.org/10.1103/PhysRevE.96.023307> 023307.
- [49] A. Putz, J. Hinebaugh, M. Aghighi, H. Day, A. Bazylak, J.T. Gostick, Introducing OpenPNM: an open source pore network modeling software package, *ECS Trans.* 58 (2013) 79–86, <https://doi.org/10.1149/05801.0079ecst>.
- [50] J. Gostick, M. Aghighi, J. Hinebaugh, T. Tranter, M.A. Hoeh, H. Day, et al., OpenPNM: a pore network modeling package, *Comput. Sci. Eng.* 18 (2016) 60–74, <https://doi.org/10.1109/MCSE.2016.49>.
- [51] J. Hinebaugh, Z. Fishman, A. Bazylak, Unstructured pore network modeling with heterogeneous PEMFC GDL porosity distributions, *J. Electrochem. Soc.* 157 (2010) B1651–7, <https://doi.org/10.1149/1.3486095>.
- [52] J.T. Hinebaugh, Pore Network Modeling and Synchrotron Imaging of Liquid Water in the Gas Diffusion Layer of Polymer Electrolyte Membrane Fuel Cells, UNIVERSITY OF TORONTO, CANADA, 2015.
- [53] J. Bear, *Dynamics of Fluids in Porous Media*, Courier Corporation, 1972.
- [54] V. Gurau, M.J. Bluemle, E.S. De Castro, Y.-M. Tsou, T.A. Zawodzinski Jr., J.A. Mann Jr., Characterization of transport properties in gas diffusion layers for proton exchange membrane fuel cells: 2. Absolute permeability, *J. Power Sour.* 165 (2007) 793–802, <https://doi.org/10.1016/j.jpowsour.2006.12.068>.
- [55] R. Banerjee, S.G. Kandlikar, Effect of temperature on in-plane permeability of the gas diffusion layer of PEM fuel cell, *ECS Trans.* 41 (2011) 489–497, <https://doi.org/10.1149/1.3635583>.
- [56] H. Oh, Lee Y. il, G. Lee, K. Min, J.S. Yi, Experimental dissection of oxygen transport resistance in the components of a polymer electrolyte membrane fuel cell, *J. Power Sour.* 345 (2017) 67–77, <https://doi.org/10.1016/j.jpowsour.2017.01.087>.
- [57] A.Z. Weber, R.L. Borup, R.M. Darling, P.K. Das, T.J. Dursch, W. Gu, et al., A critical review of modeling transport phenomena in polymer-electrolyte fuel cells, *J. Electrochem. Soc.* 161 (2014) F1254–99, <https://doi.org/10.1149/2.0751412jes>.
- [58] M. Fazeli, J. Hinebaugh, A. Bazylak, Incorporating embedded microporous layers into topologically equivalent pore network models for oxygen diffusivity calculations in polymer electrolyte membrane fuel cell gas diffusion layers, *Electrochim. Acta* 216 (2016) 364–375, <https://doi.org/10.1016/j.electacta.2016.08.126>.
- [59] J.M. LaManna, S.G. Kandlikar, Determination of effective water vapor diffusion coefficient in pemfc gas diffusion layers, *Int. J. Hydrogen Energy* 36 (2011) 5021–5029, <https://doi.org/10.1016/j.ijhydene.2011.01.036>.
- [60] H. Liu, J. Hinebaugh, S. Chevalier, R. Banerjee, C. Lee, A. Bazylak, Modeling the effect of fibre surface morphology on liquid water transport in polymer electrolyte membrane fuel cell gas diffusion layers, *Transp. Porous Media* (2017) 1–22, <https://doi.org/10.1007/s11242-017-0966-1>.